Original Article

Metallurgy in Railway Turnout and Rail Flaw Detection Techniques

Thanapol Jirasukprasert[1], Manwika Kongpuang[1,2]*, Prapas Muangjunburee[1,2], Nichapa Phrommahakul[1] and Suhaidee Sani[3]

[1]Department of Mining and Materials Engineering, Faculty of Engineering, Prince of Songkla University, Hat Yai, Songkhla 90110, Thailand

[2]Center of Excellence in Metal and Materials Engineering, Faculty of Engineering, Prince of Songkla University, Hat Yai, Songkhla 90110, Thailand

[3]Department of Industrial Engineering, Rajamangala University of Technology Srivijaya, Muang, Songkhla 90000, Thailand

*** Corresponding author, Email address: kmanwika@eng.psu.ac.th**

Abstract

Railroad tracks are considered the main component of the rail system. As a maintenance guide, track condition inspection is necessary, especially in urban or high-speed railways where material deformation must always be detected to prevent unexpected failure. This paper examined the railway turnout, which consists of several vital components that allow trains to change direction. The nose area is made of high manganese steel and has an austenitic structure, unlike a rail track with a pearlitic structure. The microstructure and work hardening mechanism have been studied. The hardness value in pearlitic rail steel increases when the lamellar spacing is more refined, with the maximum hardness found near the top surface. In the field, the austenitic structure has an original hardness of about 200HV and increases up to 600HV after

service due to the twin mechanism. Ultrasonic testing was used to investigate the possibility of flaw detection of the rails material in the lab and field.

Keywords: Railway turnout, Ultrasonic technique, Work hardening mechanism, Hadfield steel, R260 rail steel.

1. Introduction

A standard turnout consists of several parts. This type of turnout is commonly used in Thai railway tracks. Cast manganese steel, known as "Hadfield," was used to construct the area known as the "Nose" instead of the standard rail around 7-8 years ago. Due to its high toughness and work-hardening rate ranging from 180-210 HB to over 400 HB (Hodgson, 1993). The railhead at the turnout is subject to significant dynamic impact stresses as well as compressive rolling and sliding challenges. Compared to the standard rails, this section of the track is under a higher load (Kongpuang et al., 2022). Hadfield steel must thus be utilized because of its superior mechanical properties. The total strength of Hadfield steel, which has a high work-hardening rate, is enhanced by the presence of carbides (Dastur & Leslie, 1981; Ghasri-Khouzani & McDermid, 2019). The R260 steel grade is commonly used to produce the standard rails grade. The pro-eutectoid ferrite that does exist forms at the grain boundaries in this steel grade, which has a nearly entirely pearlitic microstructure, while Hadfield steel used for crossings has an austenite-grain matrix containing 11-15 in wt % Mn, with 0.8-1.25 in wt % C (Curiel-Reyna et al., 2007). Mn is an austenite stabilizer, allowing the face-centred cubic austenitic structure to stay stable at ambient temperature. Typically, the austenitic structure has difficulty with a grain structure that may quickly transition into a martensite structure.

Several papers have looked into the strengthening mechanisms of the two types of steel. Wear rates dropped with increasing hardness, lamellar spacing had an important effect on hardness, and pearlitic rail steel grade R260 was found to lower interlamellar gap. Also, harder steel had reduced or finer spacing, enhancing hardness (Lee & Polycarpou, 2005). Cleanliness improvements, inter-lamellar spacing reductions, and thick cementite lamellas can all potentially increase wear resistance (Olivares, Garcia, DeArdo, Kalay, & Hernández, 2011). Additionally, fine pearlite's increased plastic flow and fracture strain result in higher wear resistance (Korbel & Bochniak, 2017). Instability in the plastic flow of materials as a result of deformation twinning and interactions between stacking faults and dislocations Hadfield steel can undergo work-hardening in a short time (Hodgson, 1993). The increase in hardness would be approximately three times that of the initial substance (Dhar et al., 2019).

The most effective method for detecting cracks is ultrasonic testing (UT), which is not suitable for finding surface flaws until they propagate further inside (Kenderian, Berndt, Green Jr, & Djordjevic, 2003; Magel, Mutton, Ekberg, & Kapoor, 2016). At high speeds, particularly near the rail foot, surface flaws more minor than 4 mm may be overlooked as internal challenges (Ph Papaelias, Roberts, & Davis, 2008).

Therefore, this study focuses on studying the work hardening mechanism of Thai railway steel in the turnout area that affects the microstructure and hardness, allowing for early detection and prevention of potential failures. The findings from the ultrasonic inspections will be crucial in informing maintenance schedules and strategies, ensuring the longevity and safety of the Thai railway system.

2. Materials and Methods

2.1 Materials

A standard turnout consists of several parts, as shown in Figure 1. In addition to the nose area, which is made of Hadfield steel with an austenitic structure, the other rails are pearlitic rail steel. This research prepared a plate of cast manganese steel procured from manufacturing to study the work-hardening mechanism. The R260 rail steel samples were extracted from the head of a used rail section. Optical Emission Spectroscopy (OES) was used to determine the elemental composition of sample materials.

The chemical composition of the rail steel R260 (EN54E1) and Hadfield steel plate are shown in Table 1.

To study work hardening, compare the area where the sample is subjected to the wheel contact point versus the non-wheel contact area. In general, the contact position of wheels and rails can be shown in Figure 2.

2.2 Metallography

Metallographic samples were cut off using a Struers Labotom-5 and mounted on Bakelite using a Struers CitoPress-1. The samples were ground and polished using Bainpol-VT before being etched to reveal the microstructure by using 2% Nital on R260 rail steel for 5 seconds and 10ml HNO_3 + 20ml HCl + 30ml water on Hadfield steel for 7 seconds. The microstructure of the metallographic samples was evaluated using an SEM-Quanta 400-equipped.

2.3 Work-hardening of Hadfield steel

To simulate the formation of hardness, an increasing mechanism in Hadfield steel was experimented with, repeatedly hitting the specimen using a pounding hammer and checking the hardness value using the Leeb Hardness tester HT-1000A. Stop the test

when the surface hardness is close to the maximum surface hardness measured on site. Then, the sample is taken for cross-section to examine the microstructure and measure its hardness.

2.4 Hardness testing

In the laboratory, a microhardness Vicker tester MMT-X7B with a measurement unit of HV was used to measure R260 rail steel and Hadfield steel along the cross-section from the top surface down to the bottom to compare the hardness of the most impact area with base metal with no impact. On-site measurement was studied at the Hat Yai railway junction using Leeb Hardness tester HT-1000A on the turnout area. R260 rail steel measured hardness at the top of the rail and the curve of the rail head where the wheels contact, and Hadfield steel measured hardness across the entire nose area to see differences in hardness at each position.

2.5 Ultrasonic testing

Inspection of defects in railway steel using a conventional ultrasonic technique with the Ultrasonic Flaw Detector KARL DEUSCH model Digital-ECHOGRAPH Serial Number 44371 with a probe with a 45-degree angle for testing the defects of the turnout area. The graph is a scattering peak of the reflection of the ultrasonic wave signal that contacts defects in the material.

3. Results and Discussion

3.1 Work-hardening of pearlitic structures

The R260 rail steel sample shows a two-phased lamellar structure composed of alternating α-ferrite and cementite (Fe_3C) layers. As the amount of pearlite in the matrix increases, the work-hardening rate of ferrite-pearlite steel increases linearly (Pickering,

1992). Figure 3 shows the microstructure of the R260 rail steel with an almost entirely pearlitic structure. According to the SEM images, ferrite is dark, and carbide is light. The average lamellar spacing in area A is about 190.6 nm, and area B is about 120.5 nm. The lamellar spacing between the wheel contact point and the non-wheel contact point is shown in Figure 4. It corresponds to the effect of the measured hardness value, which increases when the lamellar spacing is decreased.

3.2 Work-hardening of austenitic structures

Hadfield manganese steel contains an austenite phase and carbide precipitate. As seen in Figure 5A, the carbide precipitates appear at the grain boundary, lowering ductility and increasing hardness. As a result, intergranular cracking is simpler. Due to the high Mn content, Hadfield steel has an austenitic metastable microstructure. Repeated exposure to substantial loads causes the hardness to increase relative to the original structure, exhibiting outstanding wear resistance (Fei et al., 2023; Kimura, Takemasa, & Honjo, 2011). According to Figure 5B-5E, the primary deformation processes in Hadfield manganese steel are dislocation and twinning (Kang, Zhang, Long, & Lv, 2014; Karaman, Sehitoglu, Gall, Chumlyakov, & Maier, 2000). The grain boundary twins deformation morphology is parallel straight lines passing through the grains and joining the grain boundaries, while the morphology of grain boundary carbides is either particle-like or short-rod morphology (Xu, Xia, Xiong, Lu, & Guo, 2023). The deeper layers are not subjected to significant work-hardening since the impact has little effect on the microstructure.

3.3 Hardness testing

3.3.1 Lab-Based Experiments

The lab-based hardness testing is the Microvicker hardness test by testing at the cross-section area on R260 rail steel and Hadfield steel. In the case of R260 rail steel, with a pearlitic structure, the increased surface hardness value corresponds to the reduced clearance lamellar spacing, as explained in the microstructure. The initial R260 steel hardness is 260 HBN (equivalent to 275HV) and can be increased up to 300HBN (equivalent to 320HV) after use. The result of the hardness test along the cross-section of the rail head is shown in Figure 6. It was found that the maximum hardness found at the top surface of the rail head is 350HV, and the work hardening is about 7mm deep from the surface.

A section from the Hadfield steel plate was laser cut to produce a sample with dimensions 250 mm x 20 mm x 15 mm (length x height x width) suitable for hammer testing. Hardness analysis was performed on Hadfield steel plates that had work hardening by subjecting the load repeatedly with a hammer to observe structural changes corresponding to the increased hardness value. Every 100 hits are measured with a Leeb hardness instrument until the desired hardness is about 500-600 HV, which requires manual force to smash with a hammer pound about 500 times. The results are shown in Figure 7. Hadfield manganese steel typically has a hardness of 200 HB (equivalent to 210HV) when the solution is annealed and water quenched. This material can be strain-hardened to about 500 HB (equivalent to 530HV). The work hardening is observed to extend up to a depth of around 10 mm from the running surface, and the wheel contact results in high deformation hardness of over 600 HV, approximately three times that of the as-received material. The crack path becomes wavy in this maximum hardness because most fractures pass through relatively soft grains in a direction free from the twins (Dhar et al., 2019).

3.3.2 Field-Based Experiments

Measure the hardness on-site with a Leeb Hardness tester on the R260 rail steel top surface, as shown in Figure 8. The hardness can be divided into three areas: the area in contact with the wheel flange (a), the area in contact with the wheel tread (b), and the area in contact with the fieldside (c), which has the average hardness of 300 HV, 295 HV, and 309 HV, respectively.

From measuring the hardness on site with the Leeb Hardness tester, the Hadfield steel crossing nose found three different hardness ranges, divided into ranges (a), (b), and (c), as shown in Figure 9. The test results found the lowest value equal to 452 HV in area (b), the hardness is 578 HV in area (c), and the highest hardness is 590 HV in area (a). It can be seen that the range with high hardness is located near the edge of the middle of the crossing nose. However, at the pointed end of the crossing nose at section a, the hardness range is less than that of other areas because it is an area that does not receive as much impact as other areas. The maximum hardness measure on-site of R260 is 348HV, while Hadfield steel is 590HV. The test results found that the hardness value on site is approaching the maximum hardness value of the material (BOZKURT, 2023; Dhar et al., 2019). Therefore, there should be careful inspection to prevent damage to the material.

3.4 Flaws detection using Ultrasonic testing

On-site inspection of defects in railway steel using a conventional ultrasonic (UT) technique found defects in the switch and crossing area at the wing rail in all 2 locations, as shown in Figure 10. The results obtained from inspection using the conventional ultrasonic technique are displayed as signal lines. The signal is reflected in a group of porosity distributed together, also called a group of cluster porosity. The size of the pore clusters found when compared with the standard values was within the acceptable range

following an American Railway Engineering and Maintenance-of-Way Association (AREMA) manual standard in section 4.3, which recommended minimum performance guidelines for rail testing (Manual, 2006). There is no defect found around the nose. It can be assumed in two cases that there is no internal defect or UT cannot detect defect because the austenite structure has a large grain structure, resulting in scattering of light beams from conventional UT (Bouda, Lebaili, & Benchaala, 2003).

4. Conclusions

1. With the work-hardening of R260 rail steel, it can be concluded that decreasing inter-lamellar spacing similarly increases the work-hardening rate.

2. Work-hardening of Hadfield steel results from the twinning mechanism during plastic deformation in metals.

3. The hardness obtained from both lab and on-site testing showed that the surface area was close to the maximum value of the material after work hardening, so it is important to start monitoring for possible damage.

4. Conventional ultrasonic testing is effective for detecting defects in the pearlitic or fine-grain structure but is unsuitable in austenitic or coarse structures due to beam scattering. Therefore, other techniques, such as Phased Array Ultrasonic Testing (PAUT) or Acoustic Emission Testing (AET), are more appropriate.

Acknowledgments

This research was supported by Faculty of Engineering, Academic year 2022-2023, Prince of Songkla University, Thailand and National Science, Research and Innovation Fund (NSRF). The authors are grateful to the Graduate School and the

Department of Mining and Materials Engineering, Faculty of Engineering, Prince of Songkla University, and the Center of Excellence in Metal and Materials Engineering (CEMME) for the provision of facilities, equipment, and financial support for this project.

References

BOZKURT, F. (2023). Investigation of Tribological Properties of Head, Web and Foot Sections of R260 Rail. Demiryolu Mühendisliği(17), 107-114.

Bouda, A. B., Lebaili, S., & Benchaala, A. (2003). Grain size influence on ultrasonic velocities and attenuation. Ndt & E International, 36(1), 1-5.

Curiel-Reyna, E., Contreras, J., Rangel-Ortis, T., Herrera, A., Baños, L., Real, A. d., & Rodríguez, M. (2007). Effect of carbide precipitation on the structure and hardness in the heat-affected zone of Hadfield steel after post-cooling treatments. Materials and Manufacturing Processes, 23(1), 14-20.

Dastur, Y. N., & Leslie, W. (1981). Mechanism of work hardening in Hadfield manganese steel. Metallurgical transactions A, 12, 749-759.

Dhar, S., Danielsen, H. K., Fæster, S., Rasmussen, C., Zhang, Y., & Jensen, D. J. (2019). Crack formation within a Hadfield manganese steel crossing nose. Wear, 438, 203049.

Fei, J., Zhou, G., Zhou, J., Zhou, X., Li, Z., Zuo, D., & Wu, R. (2023). Research on the Effect of Pearlite Lamellar Spacing on Rolling Contact Wear Behavior of U75V Rail Steel. Metals, 13(2), 237.

Ghasri-Khouzani, M., & McDermid, J. (2019). Modeling the Work Hardening Behavior of High-Manganese Steels. Journal of Materials Engineering and Performance, 28, 1591-1600.

Hodgson, W. (1993). Rail metallurgy and processing. Paper presented at the Rail Quality

and Maintenance for Modern Railway Operation: International Conference on Rail Quality and Maintenance for Modern Railway Operation Delft June 1992.

Kang, J., Zhang, F., Long, X., & Lv, B. (2014). Cyclic deformation and fatigue behaviors of Hadfield manganese steel. Materials Science and Engineering: A, 591, 59-68.

Karaman, I., Sehitoglu, H., Gall, K., Chumlyakov, Y. I., & Maier, H. (2000). Deformation of single crystal Hadfield steel by twinning and slip. Acta materialia, 48(6), 1345-1359.

Kenderian, S., Berndt, T. P., Green Jr, R. E., & Djordjevic, B. B. (2003). Ultrasonic monitoring of dislocations during fatigue of pearlitic rail steel. Materials Science and Engineering: A, 348(1-2), 90-99.

Kimura, T., Takemasa, M., & Honjo, M. (2011). Development of SP3 rail with high wear resistance and rolling contact fatigue resistance for heavy haul railways. JFE Techn. Rep., 16, 32-37.

Kongpuang, M., Culwick, R., Cheputeh, N., Marsh, A., Jantara Junior, V. L., Vallely, P., ... & Papaelias, M. (2022). Quantitative analysis of the structural health of railway turnouts using the acoustic emission technique. Insight-Non-Destructive Testing and Condition Monitoring, 64(7), 398-403.

Kongpuang, M. (2022). Reliability-base monitoring and maintenance of urban railway turnout using acoustic emission. University of Birmingham,

Korbel, A., & Bochniak, W. (2017). Stratified plastic flow in metals. International Journal of Mechanical Sciences, 128, 269-276.

Lee, K. M., & Polycarpou, A. A. (2005). Wear of conventional pearlitic and improved bainitic rail steels. Wear, 259(1-6), 391-399.

Magel, E., Mutton, P., Ekberg, A., & Kapoor, A. (2016). Rolling contact fatigue, wear

and broken rail derailments. Wear, 366, 249-257.

Manual, A. (2006). American Railway Engineering and Maintenance-of-Way Association.

Olivares, R. O., Garcia, C., DeArdo, A., Kalay, S., & Hernández, F. R. (2011). Advanced metallurgical alloy design and thermomechanical processing for rails steels for North American heavy haul use. Wear, 271(1-2), 364-373.

Ossberger, U., Pletz, M., Eck, S., Daves, W., & Ossberger, H. (2013). Validation of a finite element crossing model using measurements at an instrumented turnout. Paper presented at the Proceedings of the 10th International Heavy Haul Conference IHHA 2013, vol. February.

Ph Papaelias, M., Roberts, C., & Davis, C. L. (2008). A review on non-destructive evaluation of rails: state-of-the-art and future development. Proceedings of the Institution of Mechanical Engineers, Part F: Journal of Rail and rapid transit, 222(4), 367-384.

Pickering, F. (1992). Bainite in Steels. In: Taylor & Francis.

Xu, Z., Xia, Z., Xiong, Y., Lu, J., & Guo, Z. (2023). Multiple morphologies and twin structure generated by a definite growth behavior of grain boundary M23C6 in tempered Fe–15Mn–3Al-0.7 C steel. Journal of Materials Research and Technology.

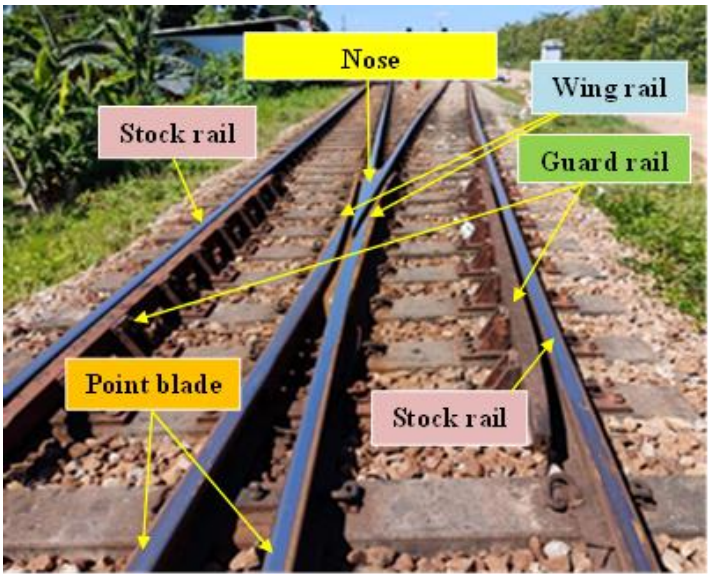

Figure 1 Standard turnout at Bangsaphanyai railway station (Kongpuang, 2022).

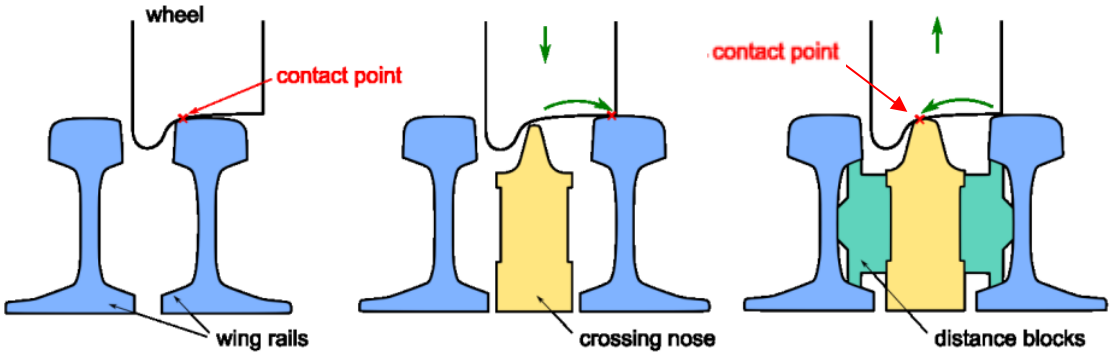

Figure 2 Illustrates the transition of the wheel from the wing rail to the crossing nose (Ossberger, Pletz, Eck, Daves, & Ossberger, 2013).

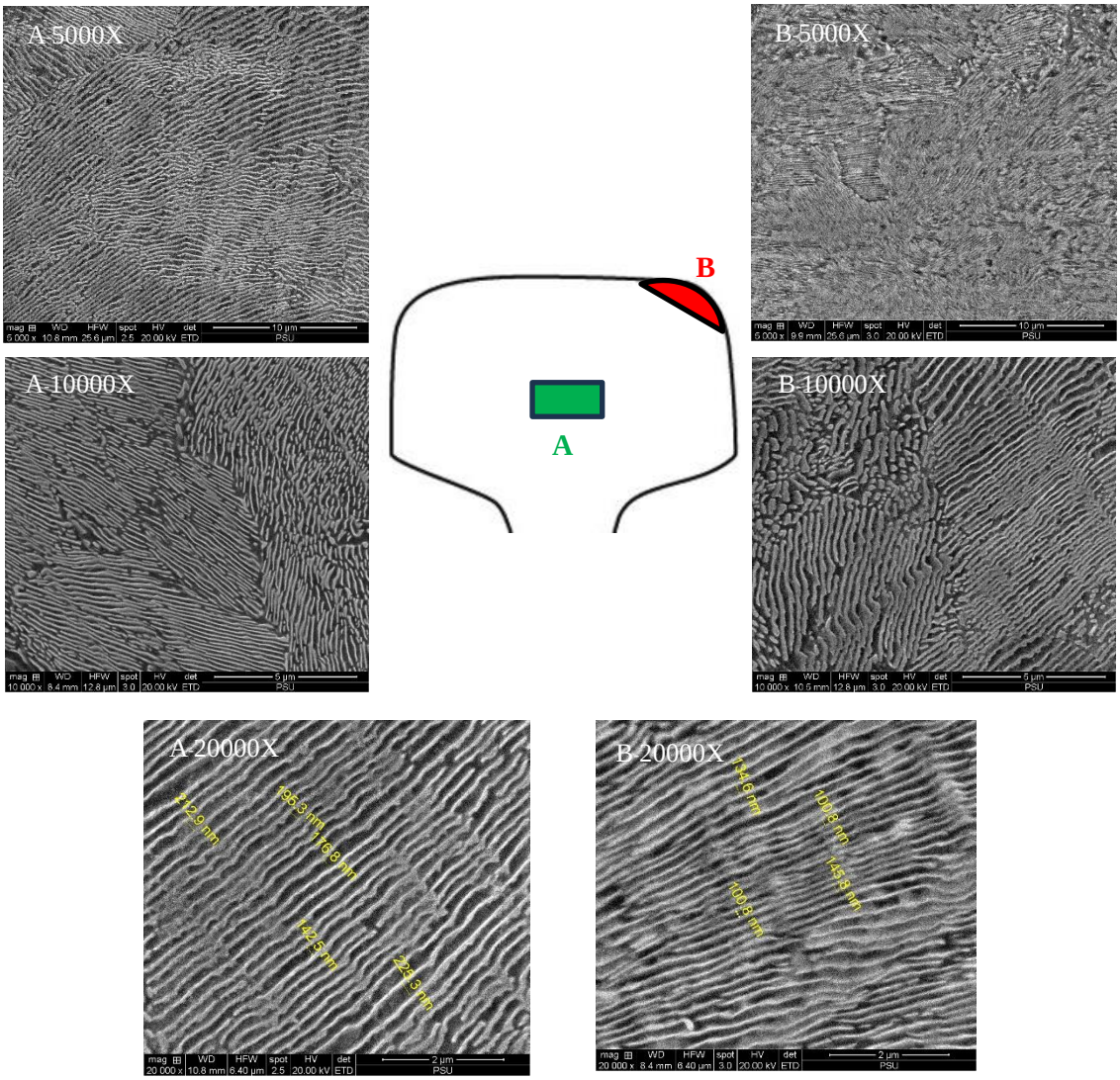

Figure 3 The Microstructure of the R260 rail steel: (A) non-wheel contact point (B) wheel contact point (critical contact zone).

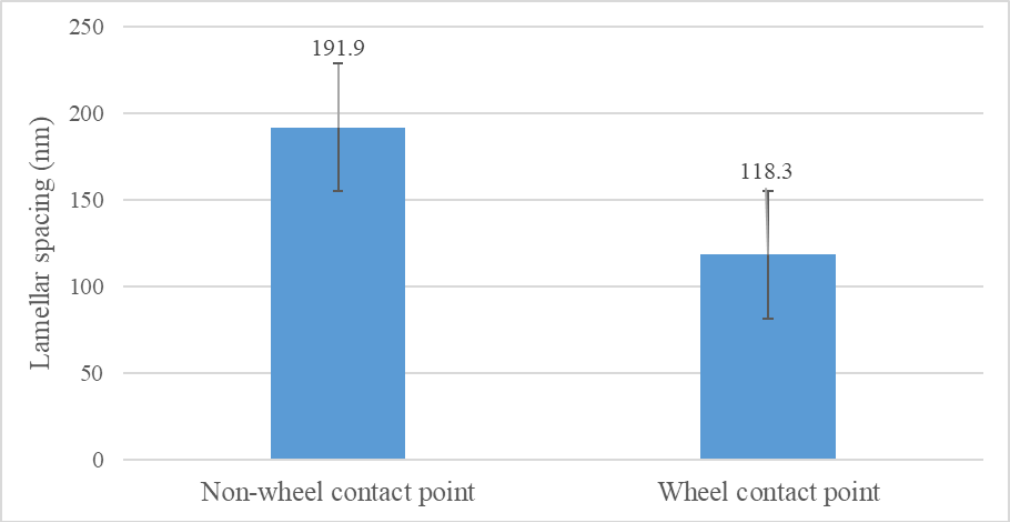

Figure 4 The lamellar spacing between the wheel and non-wheel contact points.

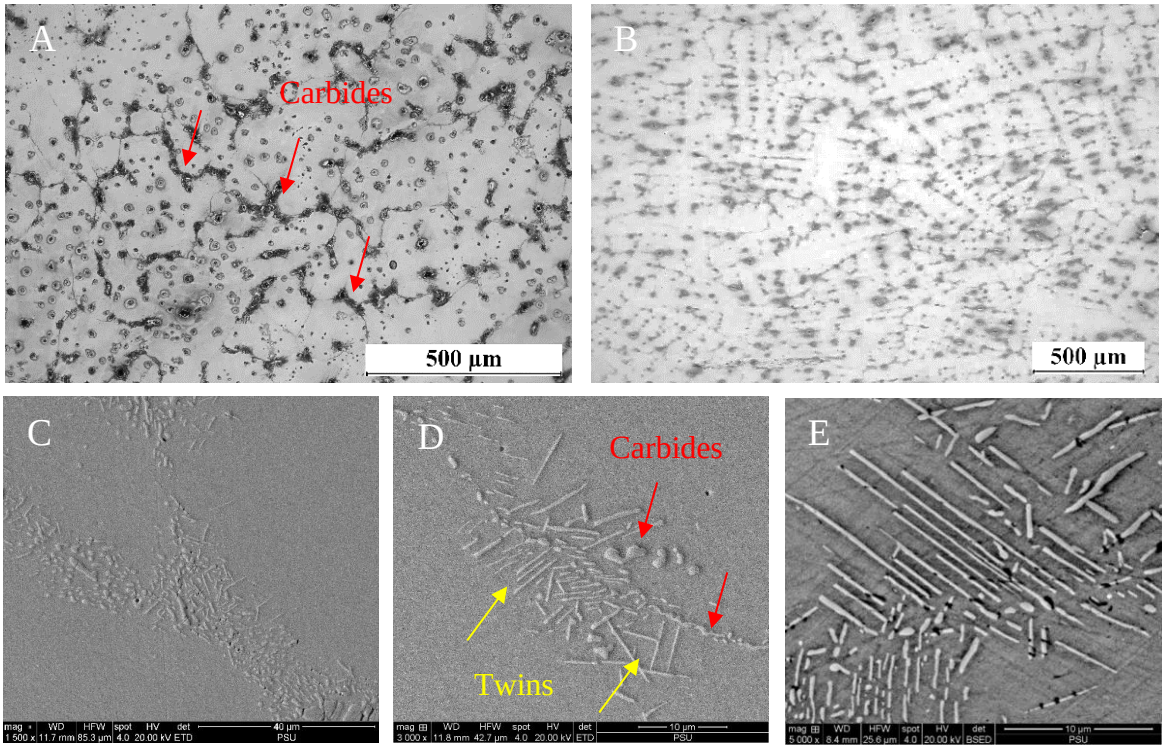

Figure 5 Microstructure of Hadfield (A) Microstructure before work hardening shows carbide along grain boundaries (B-E) Microstructure after work hardening shows short-rod morphology of grain boundary carbides and parallel straight lines of grain boundary twins deformation.

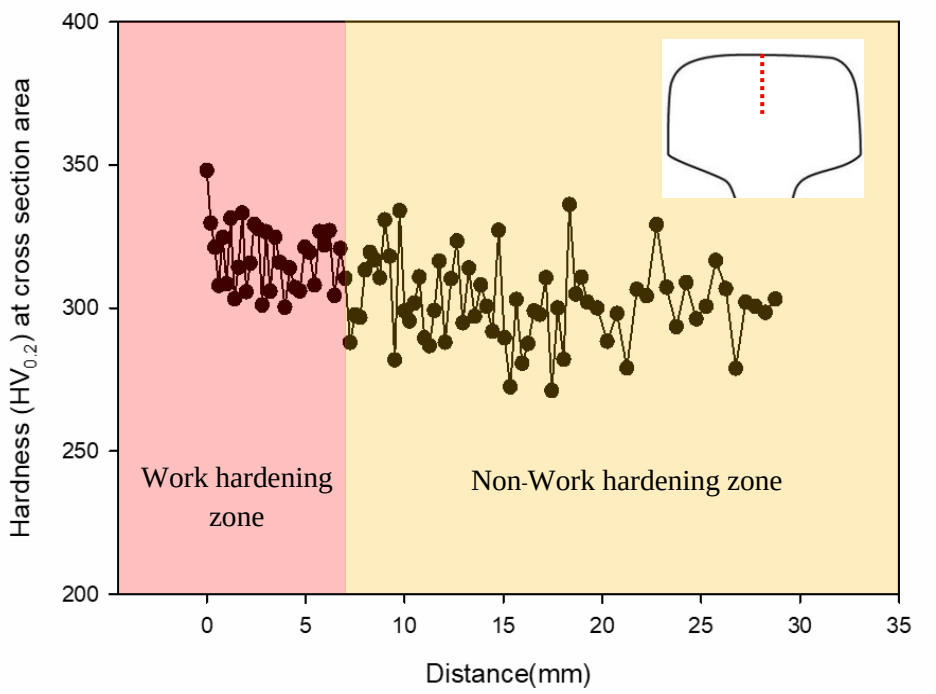

Figure 6 Hardness measurement by a cross-section of R260 rail steel.

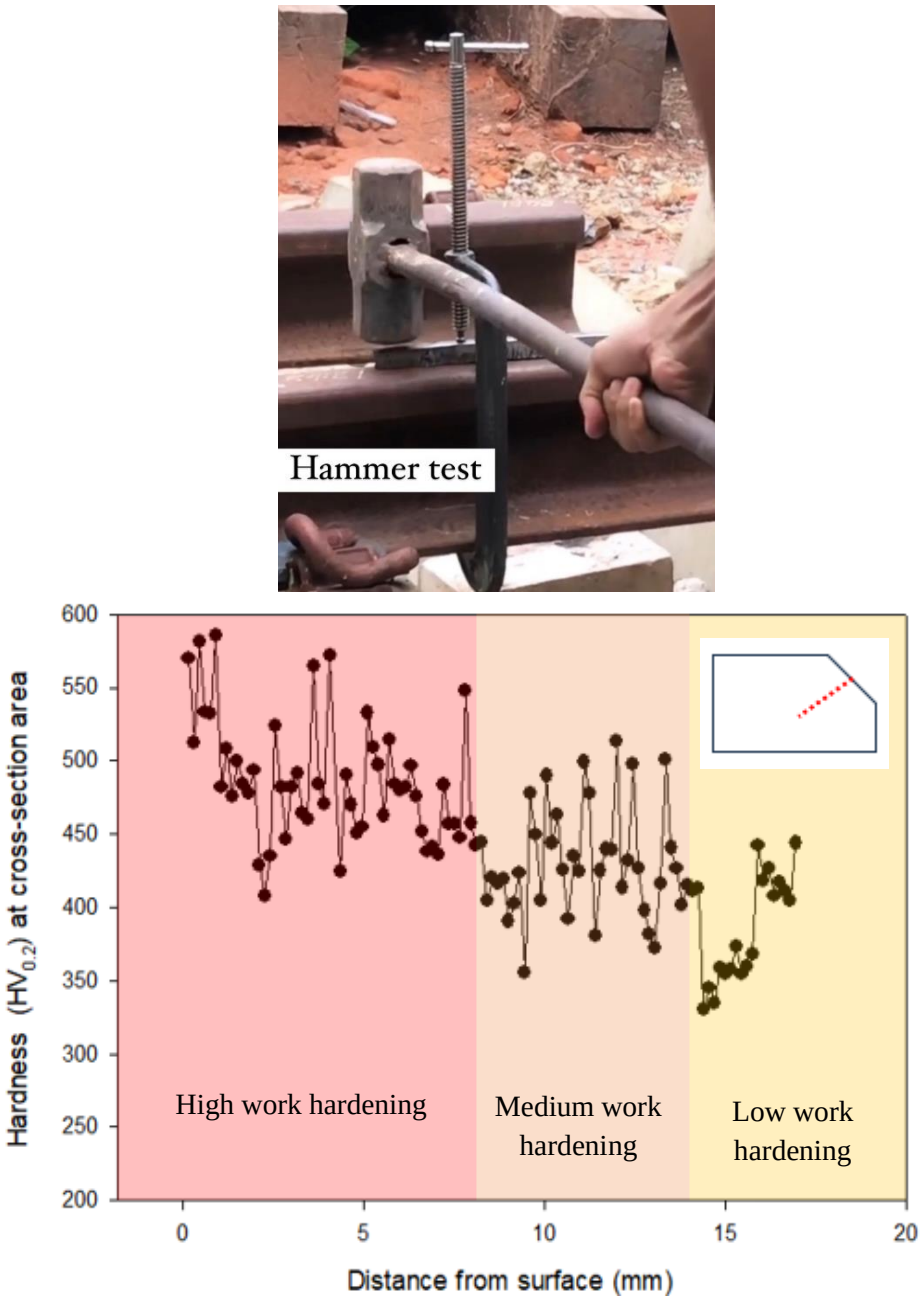

Figure 7 Hammer testing (Top) and hardness measurement of a cross-section of Hadfield steel after the test (Bottom).

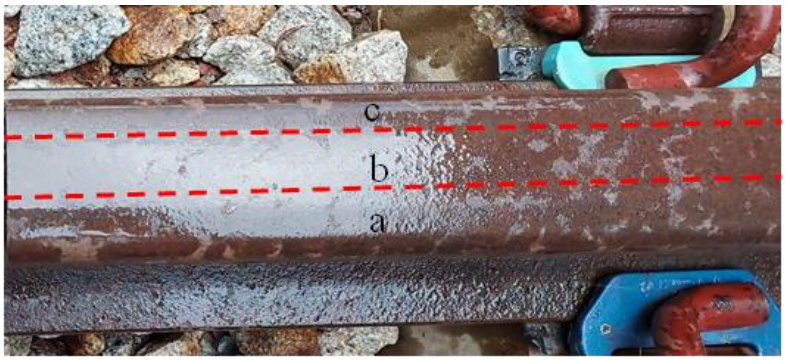

Figure 8 Field R260 rail steel with three different hardness ranges: (a) contact area with wheel flange, (b) contact area with wheel tread, (c) contact area with fieldside.

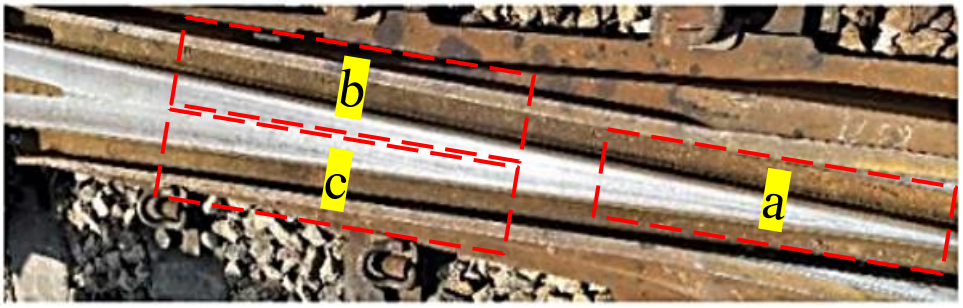

Figure 9 Crossing nose of three different hardness ranges.

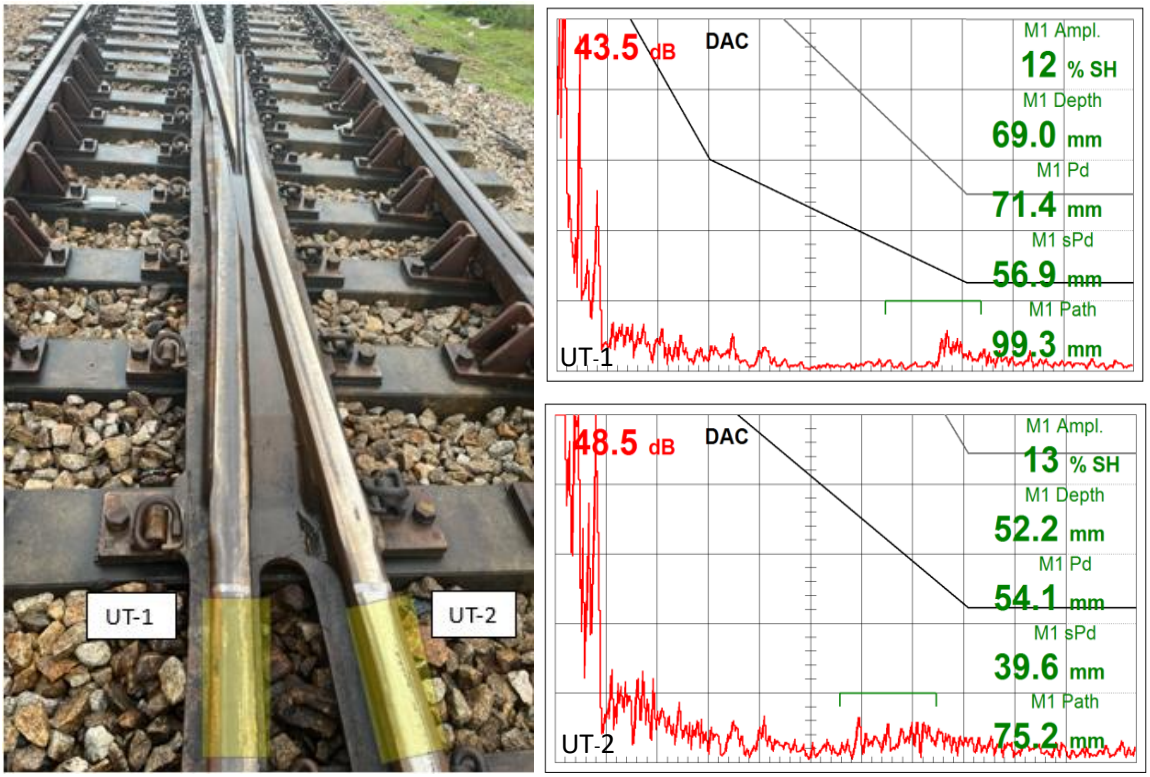

Figure 10 Location of inspection and test results for defects in rail steel at positions UT-1 and UT-2.

Materials	Chemical composition (%wt)							
	C	Si	Mn	P	S	Cr	Ni	Al
R260	0.78	0.31	0.75	0.103	0.014	0.038	-	-
Hadfield steel	1.29	0.68	14.03	0.09	0.013	1.70	0.30	0.041

Table 1 Chemical compositions of the Hadfield steel and standard rail steel R260 (in weight %).